Rheol Acta (2013) 52:767–783
DOI 10.1007/s00397-013-0709-3

ORIGINAL CONTRIBUTION

Elastic response from pressure drop measurements through planar contraction–expansion geometries by molecular dynamics: structural effects in melts and molecular origin of excess pressure drop

Jorge Castillo-Tejas · Shirley Carro · Octavio Manero

Received: 8 November 2012 / Revised: 15 April 2013 / Accepted: 16 April 2013 / Published online: 25 May 2013

Abstract In this work, we use nonequilibrium molecular dynamics to simulate a contraction–expansion flow of various systems, namely melts with molecules of various conformations (linear, branched, and star), linear molecules in solution, and a reference Lennard–Jones fluid. The equations for Poiseuille flow are solved using a multiple time scale algorithm extended to nonequilibrium situations. Simulations are performed at constant temperature using the Nose–Hoover dynamics. The main objective of this analysis is to investigate the molecular origin of pressure drop along planar contraction–expansion geometry, varying the length of the contraction, and the effect that different molecular conformations have on the resulting pressure drop along the geometry. Pressure drop is closely related to mass distribution (in neutral and gradient directions) and branching index of molecules. Also, it is shown that remarkable increases of pressure drops are also possible in planar geometries, provided large extensional viscosities combined with moderate values of the first normal stress difference in shear are considered, in addition to considerable reductions of the flow area at the contraction region.

Keywords Nonequilibrium molecular dynamics · Pressure drop · Contraction–expansion flow

J. Castillo-Tejas (✉) · S. Carro
Facultad de Ciencias Básicas, Ingeniería y Tecnología,
Universidad Autónoma de Tlaxcala, Calzada Apizaquito S/N,
Apizaco, Tlaxcala 90300, México
e-mail: j_castillo_tejas@hotmail.com

O. Manero
Instituto de Investigaciones en Materiales, Universidad Nacional
Autónoma de México, Ciudad Universitaria,
México, Federal District 04510, México

Nomenclature (variables are given in dimensionless or reduced units)

Rheological properties

η	Viscosity
σ	Stress tensor
τ	Viscous stress tensor
N_1	First normal stress function
η_0	Limiting viscosity at zero shear rate
η_s	Viscosity of solvent
$[\eta]$	Intrinsic viscosity
λ	Relaxation time
$c*$	Critical concentration
ϕ	Concentration per site
σ_{11}, σ_{22}	Normal stress components in the x_1 and x_2 directions

Dynamic properties

Q	Volume flow rate
P_0, P_1	Pressure evaluated at the beginning and end of the measurement region
ΔP	Total pressure drop
ΔP_{Entry}	Excess pressure drop originated by the reduction in flow area
$\Delta P_0, \Delta P_1$	Pressure drop under developed flow condition prior and past the contraction
ΔP_{Adim}	Relationship between the pressure drop experienced by the solution and L-J fluid
$\dot{\varepsilon} = \Delta v_1/\Delta x_1$	Strain rate
$\langle v \rangle_0$	Mean velocity of fluid at the beginning of the measurement region
E_V	Rate of dissipation
U_{NHi}	Energy removed by thermostat per particle

Geometric properties

x_1	Direction of flow
x_2	Direction of velocity gradient
x_3	Neutral direction
L_1, L_2, L_3	Length of the simulation region in x_1, x_2, and x_3 directions
Lc_1, Lc_2	Length of contraction in x_1 and x_2 directions
$\widehat{\beta}$	Contraction ratio
A_f	Flow area
N_{pz}	Number of planes perpendicular to the x_2 direction

Molecular dynamics variables

ρ	Reduced density
T	Reduced temperature
N	Total number of sites
M	Number of chains
S	Number of solvent particles
σ	Diameter (size) of particle
ε	Potential well depth
k_v	Spring constant for the FENE potential
R_0	Maximum extension of the bond for FENE potential
m_i	Particle mass
$U(\mathbf{r}^N)$	Total energy of the configuration
$U(r_{ij})$	Pair interaction energy
$U_{LJ}(r_{ij})$	Pair interaction energy in the Lennard–Jones potential
$U_{FENE}(r_{ij})$	Pair interaction energy in the FENE potential
$U(r_c)$	Energy evaluated at the cutting radius
r_{ij}	Scalar distance between particles i and j
$\mathbf{r}^N$	Position vector of the configuration
$\mathbf{r}_i$	Position vector of particle i
$\mathbf{v}_i$	Velocity vector of particle i
$\mathbf{F}_i$	Force vector of particle i
$\mathbf{F}_{Ti}$	Force associated to the thermostat for particle i
F_e	External force field
V_ζ	Thermostat velocity coordinate
ξ	Thermostat position coordinate
Q_S	Thermostat mass
L_S	Thermostat degrees of freedom
β	Reciprocal of reduced temperature

Conformational parameters

l_e	Backbone effective length of a chain
BI	Branching index
BC	Number of branches per chain
E_l	Molecular weight
$\left\langle R_g^2 \right\rangle$	Mean square radius of gyration
$\langle I_1^2\rangle, \langle I_2^2\rangle, \langle I_3^2\rangle$	Eigenvalues of mass distribution tensor in the x_1, x_2, and x_3 directions

Introduction

The contraction–expansion flow through planar or axisymmetric geometries has been a benchmark problem which allows testing available constitutive equations and new computational tools applied to different length scales. Elsewhere, we have studied the flow of linear molecules (Castillo-Tejas et al. 2009) and a Boger fluids (González-González et al. 2009) through contraction–expansion geometries with 4:1:4 and 2:1:2 ratios, respectively, using nonequilibrium molecular dynamics simulations. In the present work, two groups of fluids through a 2:1:2 contraction–expansion geometry are analyzed. Each group, with different rheological characteristics, was selected for studying (1) the effect of molecular structure on the pressure drop along the geometry and (2) the origin of the excess pressure drop. In the following, we present a discussion on the results in the framework setup in previous works related to the two issues mentioned above.

To analyze the effect of the structure of molecules on the extensional flow measured in terms of pressure drop, the contraction–expansion flow of polymer melts formed by molecules with various structures and branching indexes is simulated. It is already recognized that molecular structure as well as molecular shape are some of the important factors that dictate the rheological behavior of macromolecular systems (Jabbarzadeh et al. 2003; Woods-Adams et al. 2000). Under simple shear flow, branched molecules present large viscosity and less accentuated shear-thinning and normal stress differences (Daivis et al. 1992; Xu et al. 1995, 1997; Sendijarevic and McHugh 2000; Le Tu et al. 2009a, b). Zero shear-rate viscosity η_0 is sensitive to the branch length, and this effect decreases with increasing shear rates. At low shear rates, linear molecules adopt a more elongated ellipsoidal shape along the flow direction than that of the branched molecules, with larger concentration of segments directed along the gradient and neutral directions. This conformation induces larger degree of molecular interactions in the linear molecules than that of the branched molecules and a larger viscosity and relaxation times. The effect of branching is more accentuated at high shear rates, where the ellipsoid exhibits higher segment concentration directed along the gradient and neutral directions. The stability induced by the branches leads to a larger flow resistance than that of the linear molecules, inducing lower shear thinning, lower elasticity, and larger second normal stress coefficients Castillo-Tejas et al. (2005).

At extensional flow conditions, the extensional viscosity of branched polymers is sensitive to the presence of branching in the chain as well as to the relaxation time (Gotsis and Zeevenhoven 2004; Ogura and Takahashi 2003; Wagner 2004; Gabriel and Munstedt 2003). Apparently, branched structures present extension thickening with different magnitudes to those exhibited by linear molecules with increasing strain rate. This effect sometimes presents advantages in polymer processing (Moller et al. 2009). Neelov and Adolf (2003, 2004) used the Brownian dynamics to simulate the extensional flow of linear and branched structures. They found that the maximum chain extension, measured in terms of radius of gyration, is lower in the branched structures, and that lower degree of branching leads to higher extensional viscosity.

In addition to studying the effect of molecular structure on the pressure drop, this paper investigates the molecular origin of the *excess pressure drop*. Nigen and Walters (2002) measured the pressure drop through contraction geometries ($2 \leq \widehat{\beta} \leq 32$), in planar and axisymmetric configurations, with short and long exit dies. Contraction gap/channel width ratios of 20 or larger were used to produce a two-dimensional flow through a slit. Experiments were carried out for two Newtonian liquids and two Boger fluids. Results show no difference between the Newtonian and Boger fluids (with similar viscosity) for planar contractions. In the axisymmetric contraction, however, larger pressure drops were obtained for Boger fluids. They concluded that the excess pressure drop observed in axisymmetric geometries is associated to an increase in the size of the vortices and extensional viscosity. From molecular dynamics simulations, we show that the excess pressure drop can also be predicted in planar configurations when a suitable flow-area reduction is considered.

The absence of this phenomenon in planar geometry is due to the low elastic response of the fluid related to lower deformation rates in this geometry. This result and the relation between vortex enhancement and pressure drop have been highlighted by Walters and Webster (2003). To this respect, it was found that the strain rate experienced by the fluid depends on the type of geometry, since in axisymmetric geometries, $\dot{\varepsilon} \approx \widehat{\beta}$, while in planar, $\dot{\varepsilon} \approx \widehat{\beta}$ (Rothstein and McKinley 2001, 2002; Haward et al. 2010c). Rothstein and McKinley (1999, 2001) analyzed the flow of a Boger fluid through the contraction–expansion cylindrical geometry, for contraction ratios within $2 \leq \widehat{\beta} \leq 8$ and various curvatures for the constriction corners. Larger values of *epd* with respect to the Newtonian fluid case were found. They established that the hysteresis cycles and the dissipated energy are closely related to the pressure drop, provided that the uniform transient uniaxial extensional flow can simulate the center-line stresses and molecular conformations existing in the contraction flow. Genieser et al. (2003) found that upon increasing the contraction ratio in planar geometries, the deformation rate accumulated through the contraction increases. Additional numerical simulation contributions are numerous (see, for example, Szabo et al. 1997; Wapperom and Keunings 2001; Aboubacar et al. 2002; Alves et al. 2003; Binding et al. 2006; Aguayo et al. 2008) as well as the constitutive equations used to reproduce the kinematics and dynamics of the contraction–expansion flow. In most of these works, for Boger fluids, a decrease in pressure drop with respect to the Newtonian reference liquid is predicted. Recently (Walters et al. 2009; Tamaddon-Jahromi et al. 2011), it was found that the failure of the Oldroyd-B model to predict the correct trend in *epd* is related to a strong dependence of the first normal stress difference N_1 on shear rate (quadratic for all shear rates). For axisymmetric configurations, a valuable and clear analysis show that the prediction of excess pressure drop depends on a balance between extensional viscosity (η_E) and the first normal stress difference (N_1). These results are also consistent with those of previous works assessing the importance of extensional stresses in contraction flows (Binding and Walters 1988; Binding 1988, 1991; Lubansky et al. 2007).

In the past decade, the number of studies on the microflow of complex fluids has increased considerably, where the scale of work is of order of micrometers. Recently, Haward et al. (2010a, b, 2012a, b) reproduced the extensional flow of the dilute and semi-diluted solutions through a cross-slot micro-device for the study on stagnation points from pressure drop measurements and birefringence. Rodd et al. (2005, 2007) analyzed the flow field and excess pressure drop in the flow of the polyethylene oxide through a micro-contraction 16:1. They established that the small length scales and high deformation rates in the contraction throat lead to a significant extensional flow effect. The authors identify four flow regimes where the transition from one regime to another is detected by pressure drop measurements. Similar conclusions were obtained in other studies (Haward et al. 2010c; Li et al. 2011a, b; Lanzaro and Yuan 2011). It is important to mention that Rodd et al. (2005) shows that solutions of polyethylene oxide (PEO) exhibit a higher pressure drop than the pure solvent. However, the rheological response of these fluids indicates that the shear viscosity of PEO at 0.05 and 0.3 % is two and eight times greater than that of pure water, respectively. We believe that these differences in the viscosities are responsible for the higher pressure drop in the polymer solutions, although we are open to accept experimental evidence of edp in the planar case if these experiments show convincingly that the pressure drops measured are realized by using liquids with the same Newtonian viscosity. Similar observations can be obtained in other studies (Castillo-Tejas et al. 2009; Campo-Deaño et al. 2011).

The theoretical developments on the flow through contraction–expansion geometries include those based on continuum mechanics and, recently, on molecular dynamics. They differ in the particular spatial and temporal ranges. Molecular dynamics can reproduce the complex fluid behavior, such as abrupt changes in geometry, although the simulation scale is not directly comparable to macroscopic predictions from continuum models; nevertheless, it helps in the interpretation of rheological complex flows due to its connections with molecular structure and conformation under flow. In view of the previous suitability of the finite extensible nonlinear elastic (FENE)-CR model to simulate pressure drops in Boger fluids Tamaddon-Jahromi et al. (2010), here we use a model based on monomer springs with a FENE potential. Comparisons are made with a reference Lennard–Jones fluid. In contrast to our previous studies, in this work, the zero shear-rate viscosity is the same for the non-Newtonian fluids studied in order to have a common basis of comparison.

The manuscript is organized as follows. The "Theory and simulation method" section presents the theory and simulation method, including the equations of motion. The "Geometry and simulation method" and "Calculation of molecular properties" sections deal with the construction of the simulation region and calculation of the rheological properties. The "Simple shear flow" section includes the rheological response of fluids under simple shear flow. The "Results and discussion" section analyzes the effect of molecular structure on the extensional rheology and excess pressure drop in planar geometries. Finally, the main conclusions are presented in the "Conclusions" section.

Theory and simulation method

System of units

In real units, the length and time scales corresponding to molecular dynamics are in the order of 10^{-9} m and 10^{-12} s, respectively. Simulations within these numerical values can lead to overflow or underflow as a result of floating-point operations. To avoid this, all physical quantities are expressed in a set of dimensionless units (or reduced units), and once the properties have been measured in dimensionless units, they can easily be scaled to the suitable physical units for each problem of interest.

For molecular dynamics studies using chosen potentials based on the Lennard–Jones potential, parameters ε and σ are the most appropriate units of length and energy, to which a value of one is assigned. These, together with the bead mass ($m = 1.0$), represent the basic units of this simulation work, where all physical quantities are expressed in dimensionless (or reduced) units. Table 1 shows the relationship between m_i, ε, and σ used to express in dimensionless units the important variables used in the work. Only as a reference, Table 1 includes the conversion factors between dimensionless and real units considering a site of CH_2 groups. Note that, in this work, the chain molecules are represented according to the model of Kremer and Grest (1990), so σ, ε, and monomer mass (m) should be larger than those of a CH_2 site.

Systems under study

Five fluids are considered in this work (see Fig. 1) including linear, star, and branched structures with a density of $1.0\sigma^{-3}$, $1.025\sigma^{-3}$, and $1.03\sigma^{-3}$, respectively. Similar densities have already been used in molecular dynamics simulations of polymer solutions and melts (Castillo-Tejas et al. 2005; Busic et al. 2003), and, in this work, we take care that the systems are in the liquid state by calculating the radial distribution function (not shown). Each polymer melt is constituted by 500 chains, each one with 25 linked sites but with different molecular structure. Star polymers have a backbone effective length le of 17 linked sites, one branch with eight linked sites and with a branching index (BI) of 1.47. The branched polymer includes a backbone chain of 13 linked sites, along which six are equally spaced branches, each one bearing two segments (see Table 2), and a branching index of 11.54. It is important to mention that the branching index is defined (Jabbarzadeh et al. 2003) as $\mathrm{BI} = \mathrm{BC} * E_l \big/ l_\mathrm{e}$ where BC is the number of branches per chain, E_l is the molecular weight, and l_e is the maximum end to end distance of the chain (see Table 2). Note that the chain length is smaller than the entanglement length ($N_e = 35$) but long enough that chains exhibit Gaussian statistics (Kremer and Grest 1990).

Fluids 4 and 5 correspond to solution of linear molecules and a simple fluid constituted by spherical particles, respectively. The solution has a density of $1.05\sigma^{-3}$ including 75 linear molecules, each one with 20 linked sites, immersed in 13,500 spherical particles (the solvent). Finally, the simple fluid is made of 15,000 spherical particles with a density of $1.096\sigma^{-3}$ (see Table 3).

Molecular model

In molecular dynamics formulations, the motion of particles in the system is described by classical mechanics including particle–particle interactions. The detailed interaction among particles is given by the summation of the overall pair–pair contributions according to

$$U\left(\mathrm{r}^N\right) = \sum_i \sum_{j>i} U\left(r_{ij}\right), \tag{1}$$

Table 1 Some quantities expressed in Lennard–Jones reduced units and conversion factor between the reduced and real quantity, considering a CH_2 group as a reference site

Physical quantity	L-J unit	As a reference SI unit for CH_2
Length	σ	3.93×10^{-10}m
Mass	M	14 kg/kmol
Energy	ε	6.489×10^{-22}J
Number density	$1.0 / \sigma^3$	16.47 nm^{-3}
Temperature	ε / k_B	47 K
Time	$(m\sigma^2 / \varepsilon)^{1/2}$	2.35×10^{-12}s
Volume flow rate	$(\varepsilon\sigma^4 / m)^{1/2}$	$2.58 \times 10^{-17}m^3/s$
Stress	ε / σ^3	10.69 MPa
Viscosity	$(m\varepsilon)^{1/2} / \sigma^2$	2.51×10^{-5}kg/m s
Rate of dissipation	$(\varepsilon^3 / \sigma^2 m)^{1/2}$	2.75×10^{-10}J/s
Shear rate	$(\varepsilon / m\sigma^2)^{1/2}$	$4.25 \times 10^{11}s^{-1}$

where $U(r_{ij})$ accounts for the potential energy among pairs, and r_{ij} is the scalar distance between particles i and j. The force acting on a particle is obtained from the gradient of the potential function:

$$\mathrm{F}_i = -\frac{\partial U\left(\mathrm{r}^N\right)}{\partial \mathrm{r}_i}. \tag{2}$$

In order to reproduce the interactions between particles, two intermolecular potential are used: (1) the Lennard–Jones truncated and shifted potential and (2) FENE potential (Warner 1972). The Lennard–Jones potential is given by

$$U_{\mathrm{LJ}}(r_{ij}) = \begin{cases} 4\varepsilon\left[\left(\frac{\sigma}{r_{ij}}\right)^{12} - \left(\frac{\sigma}{r_{ij}}\right)^{6}\right] - U(r_c), & r_{ij} < r_c \\ 0, & r_{ij} \geq r_c \end{cases} \tag{3}$$

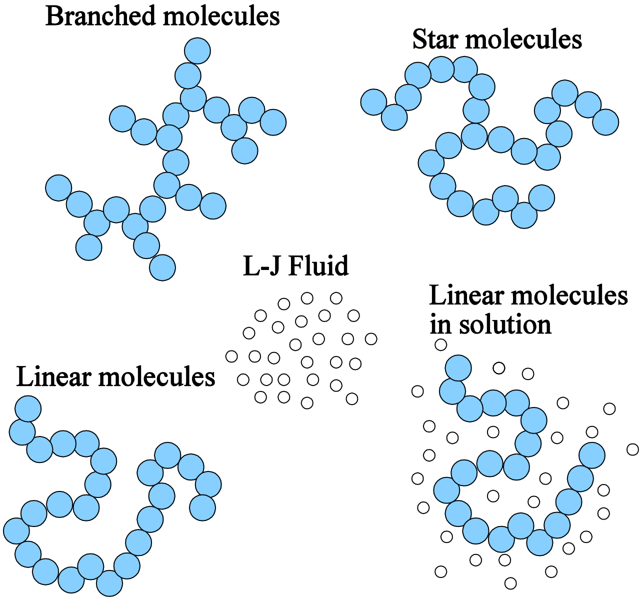

Fig. 1 Schematic representation of the systems under study

where σ is the diameter of the site, ε is the potential energy parameter, and $U(r_c)$ is the energy evaluated at the cutting radius (r_c). For all simulations in this work, the cutting radius was equal to $2^{1/6}\sigma$. It is important to mention that in this work, the force is not shifted. On the other hand, the *FENE* potential is given by

$$U_{\mathrm{FENE}}(r_{ij}) = \begin{cases} -\frac{k_v R_0^2}{2} \ln\left[1 - \left(\frac{r_{ij}}{R_0}\right)^2\right], & r_{ij} < R_0 \\ \infty, & r_{ij} \geq R_0 \end{cases} \tag{4}$$

where k_v is the spring constant equal to $100\varepsilon/\sigma^2$, and R_0 is the maximum extension of the bond equal to 1.5σ (Castillo-Tejas et al. 2005). Equations 3 and 4 represent the functional form of the intermolecular potential.

Based on Fig. 1, the molecules of the systems 1, 2, 3, and 4 are represented according to the monomer-spring model of Kremer and Grest (1990). This model considers that the molecular chain is represented by a spring, and the mass is concentrated in a monomer or site. A molecule is then envisaged as a collection of sites connected through non-harmonic springs. The attractive *FENE* potential (Eq. 4) and the repulsive part of Lennard–Jones potential (Eq. 3) reproduce conveniently the behavior of polymer solutions in confined geometries by molecular dynamics simulations. Nonadjacent sites of the molecules and spherical molecules interact with each other through the Lennard–Jones potential which contains attractive and repulsive interactions between components (Eq. 3).

Equations of motion

The contraction–expansion geometry consists in Poiseuille flow through a *planar rectangular channel* with a reduction in flow area (see Fig. 2). In molecular dynamics, the flow motion is simulated by an imposed external force F_e (Todd

Table 2 Zero shear-rate viscosity (η_0), relaxation time (λ), and information of the molecular structure of the polymer melts

Systems	Molecules	l_e	SB	BC	E_l	BI	ρ	η_0	λ
(1) Linear	500	25	–	–	25	–	1.000	28.9	147
(2) Star	500	17	8	1	25	1.47	1.025	30.1	149
(3) Branched	500	13	2	6	25	11.54	1.030	27.1	134

et al. 1995; Evans and Morriss 1990), where the particle motion is described by the following equations:

$$\frac{d\mathbf{r}_i}{dt} = \mathbf{v}_i \tag{5}$$

$$\frac{d\mathbf{v}_i}{dt} = \frac{\mathbf{F}_i}{m_i} + \frac{F_{\mathrm{e}}}{m_i}\mathbf{i} - V_\zeta \mathbf{v}_i \tag{6}$$

$$\frac{d\xi}{dt} = V_\xi \tag{7}$$

$$\frac{dV_\xi}{dt} = \frac{1}{Q_S}\left[\sum_i m_i \mathbf{v}_i^2 - \frac{L_S}{\beta}\right] \tag{8}$$

where $\mathbf{v}_i$ represents the velocity of particle i with respect to the laboratory frame of reference (i.e., the sum of the peculiar and streaming components). The peculiar velocity is the rate of change of the position of the particle under equilibrium conditions, i.e., in the absence of external perturbations. According to the geometry under study, the x_1-component of the velocity vector is affected by the imposed external force F_e; therefore, only the x_2- and x_3-component of the velocity vector develop a peculiar velocity. It is noteworthy that F_e is only applied to the input of the simulation region.

The flow motion generates viscous heat which needs to be removed from the system, so the Nose–Hoover (Nose 1984) thermostat is used to maintain the temperature constant. According to Eqs. 7 and 8, the dynamics variables of the thermostat ξ and V_ξ are the coordinates of position and velocity, respectively, and Q_S is its associated mass. Finally, L_S is the degree of freedom, and β is the reciprocal of the reduced temperature.

Geometry and simulation method

N is the total number of sites of size σ with a temperature of $3.0\varepsilon/k_B$ and reduced density (ratio of the total number of sites and simulation volume). Particles are confined in a simulation region shown in Fig. 2. Dimensions are given in units of σ. The computational region is a 2:1:2 ratio, the contraction–expansion geometry with origin located in the middle point of the domain. The length of the simulation region is estimated according to the following considerations: (1) the dimension of contraction region (Lc_1, Lc_2, and L_3) is greater than those of regions used in the simulation of the Poiseuille flow (Castillo-Tejas et al. 2005; Zhang et al. 2007), where these studies reported the behavior of bulk properties like density and radius of gyration for polymer melts; (2) L_1 should be sufficiently large for fully developed flow in the x_1-direction (13 Lc_1). Table 4 shows the dimensions in reduced units of the simulation region considering a Lc_1 / Lc_2 ratio equal to 1. In the cases of linear molecules (system 1) and the polymer solution (system 4), values of Lc_1 / Lc_2 greater than one were used. The increment in the Lc_1 / Lc_2 ratio keeps Lc_1 constant, allowing the same length in the flow direction but with smaller length along x_2. These geometrical factors permit reductions in the flow area along the contraction region, in fact simulating various orifice sizes.

To maintain longitudinal homogeneity, the external force is usually applied to all particles, as reported in other simulation works (see, for example, Todd et al. 1995; Zhang et al. 2007). However, the contraction flow is not homogeneous, so F_e is imposed only at the entry region of the simulation domain. As shown in Fig. 2, the measurement region is limited to $-0.25L_1 = x_1 = 0.25L_1$, and the external force F_e is applied to each particle positioned at the entry point of the simulation domain $m_1 = x_1 = m_2$, where $m_1 = -0.5L_1$ and $m_2 = -0.5L_1 + L_1/13$, ensuring a fully developed flow at the entry region without affecting the measurement region. The magnitude of the external force F_e varies from 0 to $7.8\varepsilon\sigma^{-1}$ and depends on the fluid type, confinement distance, density, and geometry. It is important to mention that instabilities in algorithm of integration and sometimes rupture between linked sites in the chain molecules were originated by higher values of F_e to $7.8\varepsilon\sigma^{-1}$. For linear

Table 3 Equilibrium data for the Newtonian fluid and diluted solution

Systems	Total sites	Linear chain	Sites per chain	ϕ	c*	η_0	[η]	λ	ρ
(4) Solution	15,000	75	20	0.10	0.38	6.6	3.13	62.5	1.05
(5) L-J fluid	15,000	–	–	–	–	6.5	–	–	1.096

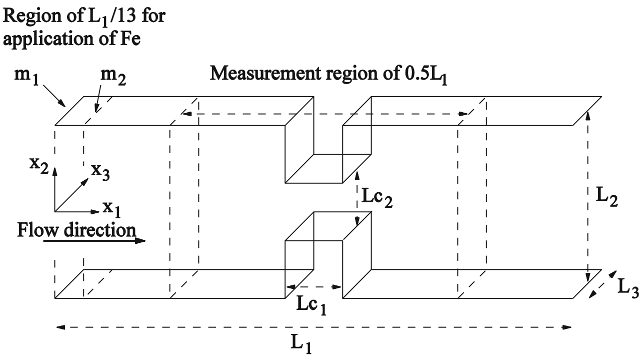

Fig. 2 Schematic representation of the 2:1:2 planar contraction–expansion geometry, whose origin ($x_1 = x_2 = x_3 = 0$) is located in the center of the contraction with dimensions of $Lc_1 \bullet Lc_2 \bullet Lc_3$

and branched chains under pressure of Poiseuille flow with a reduced density of 1, Castillo-Tejas et al. (2005) used values for F_e between $0.1\varepsilon\sigma^{-1}$ and $0.35\varepsilon\sigma^{-1}$. In the flow of linear chains and a Lennard–Jones (L-J) fluid through a contraction–expansion 4:1:4 ratio, Castillo-Tejas et al. (2009) used external forces of $0.5\varepsilon\sigma^{-1} \le F_e \le 3.5\varepsilon\sigma^{-1}$ for linear molecules and $0.125\varepsilon\sigma^{-1} \le F_e \le 1.0\varepsilon\sigma^{-1}$ for the L-J fluid with density of $0.84\sigma^{-3}$. For complex fluids through a contraction–expansion, F_e values two decades larger than those under uniform Poiseuille flow are required. However, it is important to mention that the peak velocities obtained in the previous works are similar, independent of the magnitude of the external force.

The initial configuration of particles is generated considering the entire simulation domain where particles lying in this region are equilibrated in the absence of external perturbations. Once the initial configuration is generated, the external force is imposed to produce the flow, and the minimum image and periodic boundary conditions are then applied to the flow and neutral directions (x_1 and x_3 coordinates), respectively. If the center of mass of a molecule (or spherical particles) leaves the simulation domain along the x_1 and x_3 directions, the molecule enters the region through the opposite side. It is important to mention that in the x_2-direction, fluid is confined by using stochastic walls (Rapaport 2004), such that, if a particle crosses the wall, this is repelled to the interior of the flow domain, and the effects of no slip and roughness are simulated by recalculation and scaling of the particle velocity at the objective temperature. Finally, the simulation time included two million of time steps ($\Delta t = 0.001\sigma(m/\varepsilon)^{1/2}$) for all systems.

Calculation of molecular properties

Radius of gyration $\left\langle R_g^2 \right\rangle$

Conformations of the linear, branched, and star chains (and its solutions) for various simulation conditions were analyzed. The mean-squared radius of gyration $\left\langle R_g^2 \right\rangle$ was obtained by summing the three eigenvalues ($\langle I_1^2\rangle$, $\langle I_2^2\rangle$, and $\langle I_3^2\rangle$) representing the three main axes of the ellipsoid (containing the segment distribution in the three directions) of the mass distribution tensor **G** (Rapaport 2004).

Stress tensor

In this work, the plane method for nonhomogeneous flow (Todd et al. 1995) is used to calculate the stress tensor in the fluid, according to the following expression:

$$\sigma_{\varphi\alpha}(\varphi) = \frac{1}{A}\left\langle \sum_{i=1}^{N} \frac{p_{\alpha i}\, p_{\varphi i}}{m_i}\delta(\varphi - \varphi_i)\right\rangle + \frac{1}{2A}\left\langle \sum_{i=1}^{N} F_{\alpha i}\, sgn(\varphi_i = \varphi)\right\rangle, \qquad (9)$$

where $\sigma_{\varphi\alpha}$ is the stress tensor component acting along direction α through a plane normal to the φ axis. A is the area of the plane normal to the φ axis, $\mathrm{sgn}(\varphi_i - \varphi)$ is equal to one if $(\varphi_i - \varphi) > 0$ and to -1 if $(\varphi_i - \varphi) < 0$. Furthermore, $F_\alpha i$ is the α-component of the force acting on particle i, and $p_\alpha i$ and $p_\varphi i$ are the α and φ components of the momentum of particle i, respectively. The stress tensor $\boldsymbol{\sigma}$ is related to the nonequilibrium components of the pressure tensor such that $\sigma = -\mathbf{P}$. The total stress $\boldsymbol{\sigma}$ implies the contribution of the pressure and that of the viscous stress, such that $\boldsymbol{\sigma} = -p\mathbf{I} + \boldsymbol{\tau}$. The plane method allows for the calculation of the stress components σ_{11} and σ_{22} in the computational

Table 4 Dimensionless (or reduced) lengths of the simulation region

Systems	L_1	L_2	L_3	Lc_1	Lc_2	Lc_1/Lc_2
(1) Linear 1.0/1.3	171.7	26.4/20.3	2.9/3.7	13.2	13.2/10.2	1.0/1.3
(2) Star	171.7	26.4	2.8	13.2	13.2	1.0
(3) Branched	171.7	26.4	2.8	13.2	13.2	1.0
(4) Solution	193.0	29.7/22.8/18.5	2.6/3.4/4.1	14.8	14.8/11.4/9.3	1.0/1.3/1.6
(5) L-J Fluid	193.0	29.7	2.5	14.8	14.8	1.0

domain. In molecular dynamics the total normal stress contains the nonseparable contributions from the viscous stress $\boldsymbol{\tau}$ and pressure $p\mathbf{I}$.

Rate of dissipation

The pressure drop is directly related to the viscous dissipation term $-\boldsymbol{\tau} : \nabla\mathbf{v}$. It is important to establish the molecular origin of the rate of viscous dissipation along the contraction–expansion geometry. The viscous dissipation induces an increase in temperature and in the velocity gradients. An important assumption considers that the heat removed by the thermostat is equivalent to that arising from the temperature increase by viscous dissipation, in order to maintain the temperature constant. The expression for the viscous dissipation is given by an integral over the entire system volume so $E_v = -\int_V (\tau : \nabla v) dV$ where $\boldsymbol{\tau}$ is the stress tensor and $\nabla\mathbf{v}$ is the velocity gradient. Considering that the stress field is the same in the fully developed flow regions upstream and downstream the contraction, Szabo et al. (1997) suggested that the rate of dissipation E_v is related to the pressure drop by

$$E_v = \Delta P Q. \tag{10}$$

Now, the force associated to the thermostat $\mathbf{F}_{Ti}$ (see Eq. 6) is given by $F_{Ti} = -m_i V_\xi v_i = -\nabla U_{NHi}$, where U_{NHi} is the energy removed per particle i. The rate of change of the energy removed per particle is then given by

$$\frac{\partial U_{NHi}}{\partial t} = m_i V_\xi v_i^2. \tag{11}$$

Equation 11 is used to estimate the rate of energy removed by thermostat in the flow direction. Considering that the thermostat removes or adds heat, even under equilibrium, the rate of energy removed under flow is obtained after subtracting that under equilibrium ($F_e = 0$). It can be demonstrated that the amount of energy that the thermostat removes (given by Eq. 11) to maintain a constant temperature is equivalent, as a first approximation, to the rate of dissipation (given by Eq. 10).

Simple shear flow

Simulations were performed in a range of dimensionless shear rates of 0.001 to 1.0 according to the conditions shown in Tables 2 and 3. Simple shear flow was simulated using the method SLLOD (Evans and Morriss 1990), where the temperature was kept constant by coupling the equations of motion to the Nose–Hoover thermostat. The variation of dimensionless shear viscosity (η) and dimensionless first normal stress difference (N_1) as a function of shear rate ($\dot{\gamma}$) are shown in Figs. 3 and 4, respectively, for all fluids. It is important to mention that reduced values of shear rate are similar to those used in other studies (see, for example, Xu et al. 1995); however, reduced shear rates reached in the simulation are usually two or three orders of magnitude higher than those commonly found in polymer processing (see Moore et al. 2000). Figure 3 shows the results for polymer melts composed of the linear, star, and branched molecules. The first Newtonian region is located in the range of $0.0002 \le \dot{\gamma} \le 0.005$. For reduced shear rates larger than 0.005, shear-thinning viscosity is apparent; the slope of −0.39 is consistent with data reported for polymer melts (Bird et al. 1987). The interplay between molecular interactions and molecular structure largely determines the rheological behavior of chain molecules. For example, branched molecules have a slightly lower η_0 than those of linear and star molecules (see Table 2), but in the shear-thinning region, the viscosity of linear molecules is lower than that of branched molecules. It is important to mention that the density of these systems was selected to exhibit a

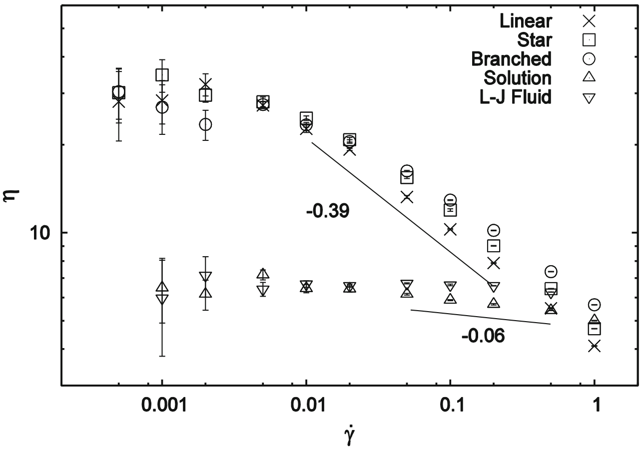

Fig. 3 Reduced shear viscosity η versus shear rate $\dot{\gamma}$ for polymer melts, diluted solution and L-J fluid

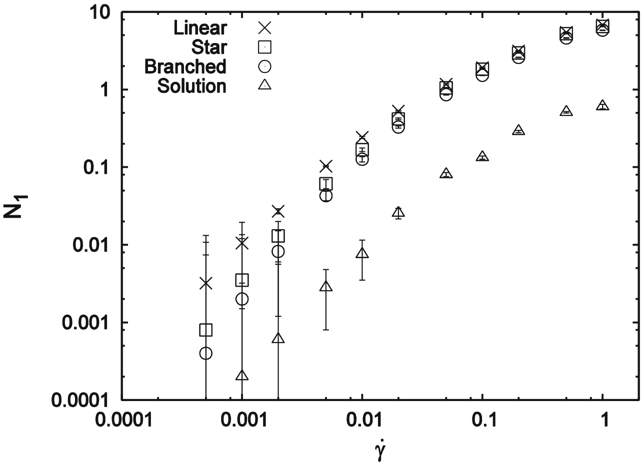

Fig. 4 Reduced first normal stress difference N_1 versus shear rate $\dot{\gamma}$ for polymer melts and diluted solution

similar zero shear-rate viscosity η_0 but ensuring that they are in the liquid state. In Fig. 4, N_1 (dimensionless first normal stress difference) grows with reduced shear rate initially with quadratic dependence on shear rate but the slope lower as the shear rate increases. This variation of N_1 with reduced shear rate is suitable to obtain an increasing *epd*, as mentioned by Walters et al. (2009). Table 2 also lists the relaxation times of these fluids which were calculated according to $\lambda = 6E_l\eta_0 \big/ \pi^2\rho T$ where E_l is the number of segments per chain.

The solution of linear molecules with concentration per site (ϕ) equal to 0.10 was considered for pressure drop simulations. The concentration per site ϕ is the ratio of the solute number of sites and the total number of sites (solute and solvent). This concentration is the same to that used elsewhere (González-González et al. 2009) and was selected to ensure a dilute regime according to the value of the critical concentration (c*). In reduced units, c* is given by $c* = 3E_l \big/ 4\pi R_g^3$ where R_g is the radius of gyration obtained from the equilibrium molecular dynamics. Although molecular size and shape obtained from the radius of gyration and its eigenvalues depend on the selected model, the ratio of the eigenvalues $\left[I_1^2/I_3^2 \ : \ J_2^2/I_3^2 \ : \ I_3^2/I_3^2\right]$ is known to be independent of this choice. For polymeric solutions, this ratio is [14.8 : 3.06 : 1.0], predicted by the "self-avoiding random-walk" model (Mazur et al. 1973). The solution has an eigenvalue ratio of [15.0 : 3.3 : 1.0]. For the polymer solution, Fig. 3 exhibits a Newtonian region extending to reduced shear rates around 0.02 with a slight shear-thinning region with slope of -0.06. In Fig. 4, the solution of linear molecules exhibits a quadratic dependence on shear rate at low shear rates, thereafter a weak dependence on shear rate is predicted. The shear viscosity is almost constant for the reference fluid modeled by the Lennard–Jones potential.

Results and discussion

The first part of this section analyzes the flow of the linear, star, and branched polymers to identify the effect of molecular structure on the pressure drop. The second part deals with the flow of the solution of linear molecules and the L-J fluid, with different Lc_1 / Lc_2 ratios to characterize the behavior of excess pressure drop (*epd*). It is important to mention that the flow through the contraction–expansion geometry (see Fig. 2) corresponds to a planar flow. This condition is guaranteed by the application of the periodic boundary conditions and minimum image concept in vorticity direction which lead to considering an infinite length along this direction. Additionally, it is verified that the v_3-component of the velocity vector be zero (peculiar velocity), with no dependency with the x_3-coordinate.

It is noteworthy that properties estimation is performed after the system has reached equilibrium (Haile 1997), ensuring that the profile of the property of interest does not change with time. Results were obtained for a number of time-averaged fluid properties where the properties examined here are stress, radius of gyration, velocity profiles, and rate of energy removed by thermostat in the test region. To determine an average property, we divide the test region into a sufficient number of slices (for velocity, radius of gyration, and rate of energy removed by thermostat profiles) or planes (for stress profiles). Then, we calculate the time-averaged property for each slice or plane. For example, we add the x-component of the particle velocities in each slice, and then we average over the number of particles in that slice at each time step. Finally, the velocity profile is obtained by computing the time average velocity for each slice during the simulation. Similar considerations are made for the stress profiles.

Total pressure drop (ΔP)

The plane method is used here to estimate dimensionless normal component of the stress tensor σ_{22}. To calculate σ_{22}, a number of planes N_{pz} normal to the x_2-direction are placed along the central symmetry line ($x_2 = 0$). Each plane has a length along the flow and neutral directions of $0.5L_1$ / N_{pz} and L_3, respectively. The calculation of the σ_{22} component includes the contribution of the pressure and viscous stress $\sigma_{22} = p + \tau_{22}$, the latter originated by the velocity gradients. The pressure profiles were obtained as a function of dimensionless axial coordinate (x_1) and reference flow rate (Q) obtained by the product of the average velocity of the fluid before the contraction ($< \ v \ >_0$) and the flow area ($A_f = L_2L_3$).

Figure 5 shows the pressure profiles for the five fluids, with a Lc_1 / Lc_2 ratio of 1, and the pressure profiles of the linear polymer and polymer solution with ratios larger than 1. It is noteworthy that each point in the pressure profile represents the calculation of σ_{22} on a plane x_1x_3, such that the pressure profile consists of 30 and 50 points for polymers melts and solutions, respectively. Pressure is the only property with estimation error which it is not shown in the figure for clarity. However, the standard deviation of the average pressure per plane, estimated by the Flyvbjerg and Petersen method (Flyvbjerg and Petersen 1989), was less than 0.5 %. At the beginning of the measurement region, for Lc_1 / $Lc_2 = 1$, the linear, star, and branched polymers have dimensionless pressure values of 16.30, 19.60, and 23.78, respectively, and just before the contraction, the polymers experience a linear decrease in pressure, with a slope depending on molecular structure. Within the interval $-41.4 = x_1 = -11.8$, the slope of the pressure lines is 0.05 for the linear polymer and 0.13 for the branched

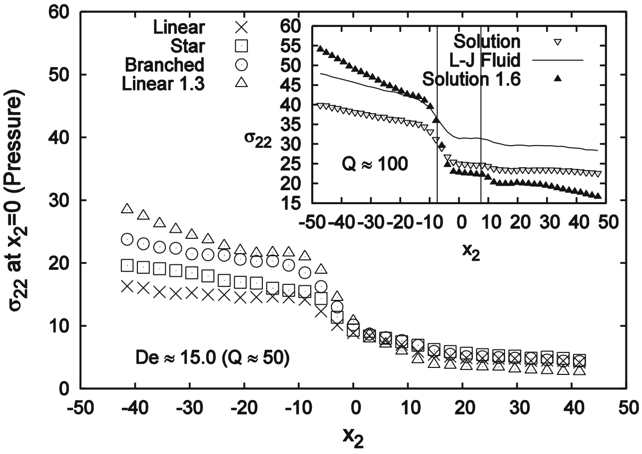

Fig. 5 Variation of reduced normal stress σ_{22} (or pressure), evaluated at the center line of confinement, as a function of the axial coordinate x_1 for fluids under study

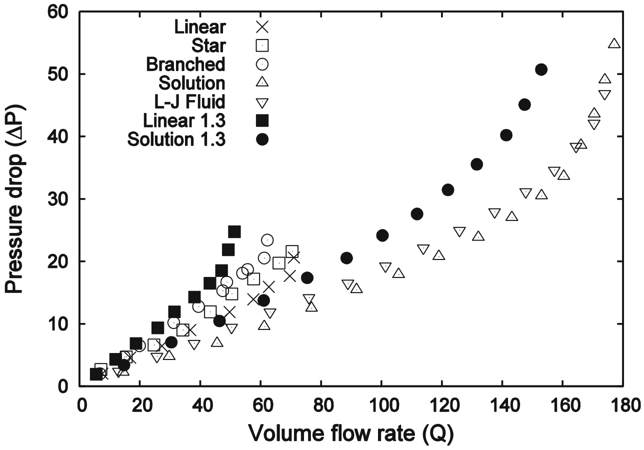

Fig. 6 Reduced pressure drop ΔP as a function of the volume flow rate Q for polymer melts, diluted solution and L-J fluid

molecules, showing that the molecules with branch index other than one develop larger pressure drops. Outside the contraction, reduced pressure values are similar in the three cases (around 4). As the ratio Lc_1 / Lc_2 increases to 1.3, in the linear molecules, the pressure profile changes drastically. It has a value of 28.45 at the beginning of the measuring region, and upon approaching the contraction, the pressure loss has a slope of 0.31, a six times larger than in the case with Lc_1 / Lc_2 = 1. The pressure profile for the linear polymer with Lc_1 / Lc_2 = 1.3 exhibits a slight increase in $x_1 = -14.8$, which is consistent with results obtained by Aguayo et al. (2008) using continuum models for Boger fluids. Apparently, this increase in the pressure profile exhibited by the linear molecules before the contraction depends on molecular structure and geometry. Again, the largest pressure drop occurs at the entry region, while at the expansion region, pressure continues to decrease linearly for Lc_1 / Lc_2 = 1.3. In the inset of Fig. 5, pressure profiles for the solution and L-J for Lc_1 / Lc_2 = 1 have similar slopes, although a larger drop is observed in the solution for Lc_1 / Lc_2 = 1.3. Before the contraction, values of the slopes are 0.19 and 0.16, and at the expansion, these are 0.04 and 0.03 for solution and L-J, respectively. Upon increasing Lc_1 / Lc_2 for the solution, the slope increases from 0.16 to 0.38.

Reduced total pressure drop ($\Delta P = P_0 - P_1$) was calculated at the beginning (P_0) and end (P_1) of the test region (planes located at $x_1 = \mp 0.25L_1$). Figure 6 exhibits the total pressure drops for all fluids when Lc_1 / Lc_2 = 1.0, showing larger pressure drops in the melts. The maximum values reached for the external force F_e were $7.0\varepsilon\sigma^{-1}$ and $6.4\varepsilon\sigma^{-1}$ in the melts and solution, respectively, although the flow rates are smaller, as expected. In Fig. 6, attention is given to the branched molecules with similar dimensionless zero shear-rate viscosity (η_0) but with different branching index ($BI = 11.54$). These molecules exhibit larger pressure drops which increase linearly with flow rate Q. In the interval $7 = Q = 50$, ΔP varies from 2.03 to 11.9 in the linear molecules, from 2.69 to 14.8 in the star molecules, and from 2.01 to 16.7 in the branched molecules. In contraction–expansion geometries, the pressure drop is related to the resistance to strain rate, i.e., the extensional viscosity (Binding 1991), and the important geometrical parameter is the ratio Lc_1 / Lc_2. In the linear molecules, an increase in Lc_1 / Lc_2 from 1.0 to 1.3, ΔP increases from 11.9 to 21.9 when the flow rate is 50. This result is relevant in polymer melts, since by changing the ratio Lc_1 / Lc_2 or reducing the contraction flow area, similar pressure drops can be obtained in melts with dissimilar molecular structure.

It is remarkable that these predictions are in qualitative accord with experimental data of Boger fluids through porous media (Campo-Deaño et al. 2012). Indeed, in the data for all packed beds, the variation of the pressure drop at low interstitial velocities is linear, as what happens for Newtonian fluids. For increasing velocity and above a critical value, the slope increases due to elastic effects. This is precisely observed in the pressure drop versus the flow rate predictions shown in Fig. 6. For low flow rates, an initial linear region is apparent. Of course, the initial slope of these curves along this region is proportional to the viscosity. For increasing flow rate, the nonlinear increase in the pressure drop reveals an onset for elastic effects, which is presumably related to molecular structure. In the linear molecules, elastic effects appear at higher flow rates than those of the other molecules. In this case, the enhancement in pressure drop is likely to be compensated by the largest shear thinning (see Fig. 3). As expected, the onset for elastic effects appears at lower flow rates as the ratio Lc_1 / Lc_2 changes from 1 to 1.3.

In Fig. 6, the solution and the L-J fluid exhibit similar pressure drops (from 2.4 to 49) in the range of $14 = Q = 177$. This result is consistent with experimental data in planar contractions (Nigen and Walters 2002) with various contraction ratios ($\widehat{\beta}$) and length-to-height ratio (L / a) analogous to the ratio Lc_1 / Lc_2. For example, for $\widehat{\beta} = 4 : 1$, L / a is 14.29. In Table 4, the ratios Lc_1 / Lc_2 considered for the dilute solution are 1.0, 1.3, and 1.6, which have the most important effect on the pressure drop. Note that L-J Fluid exhibits a change in the slope as a non-Newtonian fluid. Non-Newtonian behavior in simple fluids characterized by a Lennard–Jones potential has already been reported (Delhommelle et al. 2003, 2004). All these results seem to suggest than the L-J fluid is not particularly suitable to describe the rheological behavior of a Newtonian solvent. In Fig. 3, as a first approximation, we consider that the L-J fluid is nearly Newtonian. In Fig. 6, the solution of linear molecules in a geometry with a ratio of Lc_1 / Lc_2 = 1.3 experiences larger pressure drops than those of a L-J fluid with Lc_1 / Lc_2 = 1.0. This comparison identifies the effect of reduction in the flow area on the *epd* experimentally observed in axisymmetric geometries (Nigen and Walters 2002; Rothstein and McKinley 1999, 2001). The present predictions reveal a large effect in area reduction on the pressure drop in planar geometries as well.

An additional objective of this study is to demonstrate the equivalence between the rate of dissipation (E_v) and removal of energy by the thermostat (U_{NHT}), when fluids flow through a contraction-expansion geometry. In Fig. 7, the rate of dissipation and energy removed by the thermostat as a function of flow rate are disclosed for linear and branched polymers, and for the dilute solution. Calculation of U_{NHT} involves cells (Nc) where Nc is equal to 23 and 50 for melts and solution, respectively, within the calculation domain of $-0.25L_1 = x_1 = 0.25L_1$. For each cell ($1 \ldots Nc$), the particle contribution ($\partial U_{NHi} \big/ \partial t$) is used with Eq. 11 to estimate the rate of energy removal per cell $U_{NH}(k)$. For example, for cell number one located at beginning of test region, U_{NH} (1) is given by $U_{NH}(1) = \sum_{i=1}^{Np} \partial U_{NHi}/\partial t$, where Np is the number of particles in cell number one. Values shown in Fig. 7 are obtained using $\sum_{k=1}^{Nc} U_{NH(k)}$. Calculation of E_v involves values of the total pressure drop ΔP and flow rate Q in Fig. 6. For equal intervals of Q, the rate of energy removal in the thermostat (U_{NHT}) is larger in the branched molecules than that of the linear molecules and dilute solution, which is consistent with the pressure drop exhibited forLc_1 / Lc_2 = 1. Results of E_v and U_{NHT} show close agreement, since the mean departure, defined as $100 * |E_v - U_{NHT}| \big/ E_v$, is 3.46, 6.67, and 20 % for the linear, branched molecules, and the solution, respectively. We like to emphasize that this is a first approximation to the equivalence of E_v and U_{NHT} for this geometry. The equivalence further ensures the correct thermostat operation according to energy conservation. In apparent consistency among predictions shown in Fig. 7, the pressure drop ΔP is closely related to the rate of removed energy (U_{NHT}). An apparent advantage representing Eq. 11 is that the rate of dissipation can be estimated in every point of the flow domain, which enables one to grasp the causes that originate the pressure losses along complex trajectories. Having demonstrated the equivalence between E_v and U_{NHT}, U_{NHT} will be named the *rate of dissipation* in the rest of the paper.

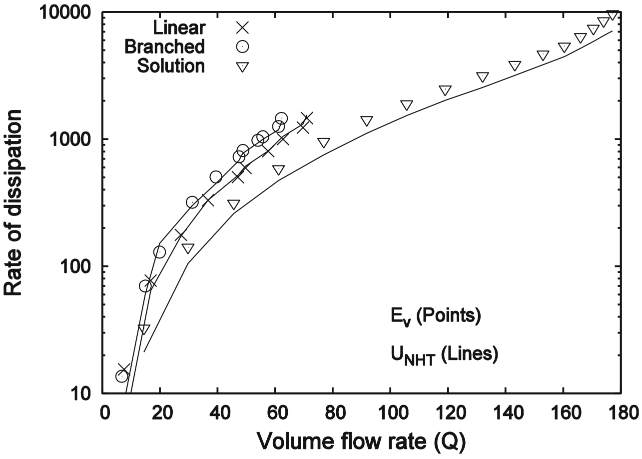

Fig. 7 Reduced rate of dissipation E_v and rate of removed energy by thermostat U_{NHT} as a function of the volume flow rate Q for linear and branched polymers, and for solution of linear molecules

Extensional rheology of melts

Here, we analyze the pressure drop, deformation, and shape of the three molecular structures at the same flow rate (Q). In Fig. 8 Lc_1 / Lc_2 = 1.0. the derivative ΔP / Δx_1 and the rate of dissipation per cell $U_{NH}(k)$ are shown as functions of the axial coordinate x_1 for the three melts. In Fig. 8a, the pressure gradient ΔP / Δx_1 prior the contraction is the largest in branched molecules. A peak is located at the contraction entry, and inside the contraction, the gradient diminishes almost to zero. The first peak depends on molecular structure, being the largest for branched molecules, followed by the star molecules. A second peak of ΔP / Δx_1 in melts at the contraction exit is shown. In the inset in Fig. 8a (Lc_1 / Lc_2 = 1.0, 1.3), the pressure gradient ΔP / Δx_1 in linear molecules increases from 0.63 to 1.47 at the contraction entry. Note that ΔP / Δx_1 is negative for the linear polymer at $x_1 = -29.6$, implying that the pressure at that point is larger. In Fig. 8b, the rate of dissipation profiles shows striking similarities with the pressure profiles, i.e., a first peak at the entry region followed by an almost zero value inside the contraction and a second peak at the exit. The rate of dissipation at the entry of the contraction is 162.0,

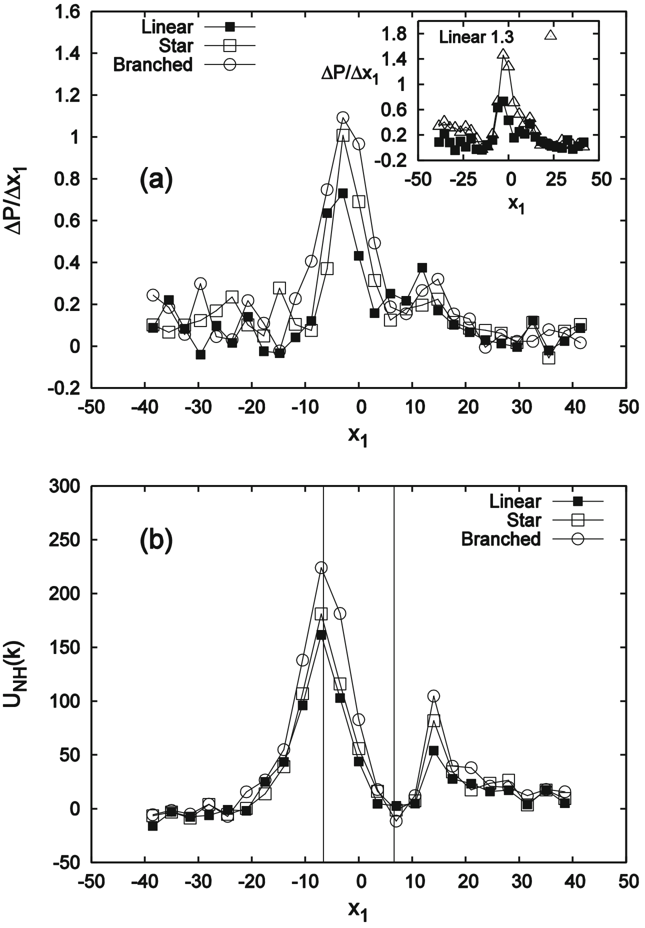

Fig. 8 **a** Variation of reduced pressure gradient ΔP / Δx, and **b** reduced rate of dissipation $U_{NH}(k)$, as a function of the axial coordinate x_1 for polymer melts at $Q \approx 50$

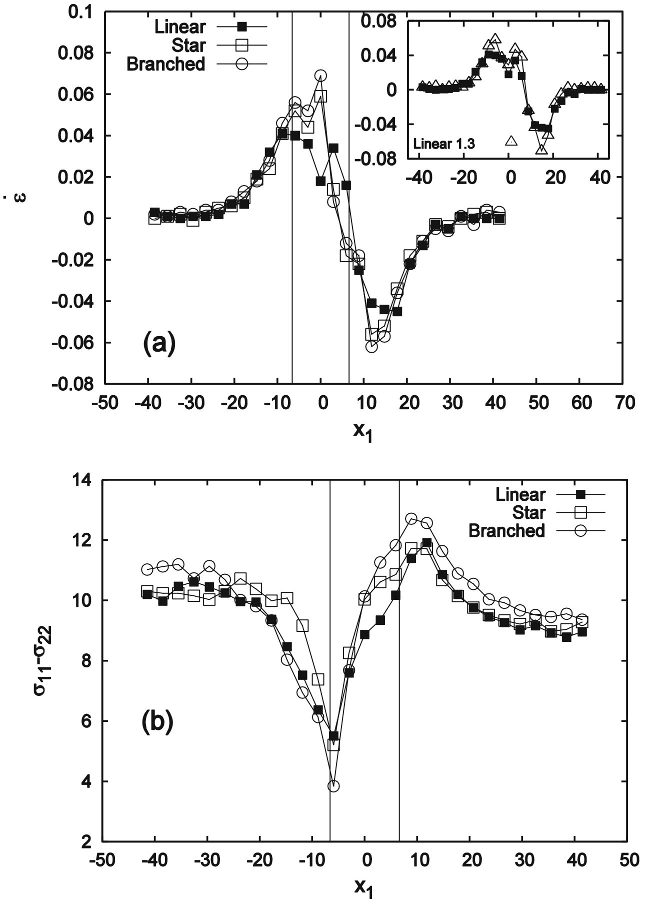

Fig. 9 **a** Variation of reduced strain rate $\dot{\varepsilon} = \Delta v_1/\Delta x_1$, and **b** reduced stress difference $\sigma_{11} - \sigma_{22}$, as a function of the axial coordinate x_1 for polymer melts at $Q \approx 50$

181.0, and 224.0 for the linear, star, and branched polymers, respectively. The rate of dissipation per cell $U_{NH}(k)$ is then associated to both the value of the pressure and pressure gradient itself. Note that $U_{NH}(k)$ is negative in the interval $-38 \leq x_1 \leq -21$ which may be associated to additional heat introduced by the thermostat in that region.

To elucidate the contribution of the extensional stress σ_{11} associated to strain rate, in Fig. 9, $\dot{\varepsilon} = \Delta v_1 \big/ \Delta x_1$ is plotted along the central symmetry line. Before the contraction, similar values of strain rate are shown, while inside the contraction, a maximum is attained, with values of 0.05, 0.08, and 0.09 for the linear, star, and branched molecules, respectively. Past the contraction, the gradient attains a minimum value within $10.0 \leq x_1 \leq 20.0$ depending on the molecular structure. Thereafter, $\dot{\varepsilon}$ increases up to zero at x_1 30.0 for all structures. The extensional viscosity, in turn, should first decrease at the contraction entrance, but inside it, a drastic increase occurs, since the stress overshoots and the gradient goes through a minimum. It is important to note that peaks in the rate of dissipation $U_{NH}(k)$ shown in Fig. 8b coincide with the peaks in $\sigma_{11} - \sigma_{22}$ and gradient $\dot{\varepsilon} = \Delta v_1 \big/ \Delta x_1$ shown in Fig. 9.

The extensional flow generated at the contraction entry and exit zones produce a deformation–relaxation process of the molecular conformation. In Fig. 9b, the stress difference $\sigma_{11} - \sigma_{22}$ is plotted with axial distance x_1 following a trajectory along the central symmetry line. Within the interval $-41.44 \leq x_1 \leq -20.0$ the branched molecules exhibit the largest stress difference $\sigma_{11} - \sigma_{22} = 4.81$. At $x_1 = -20.0$, $\sigma_{11} - \sigma_{22}$ goes through a minimum at the contraction entry zone ($x_1 = -6.6$). Collisions among the molecules result in a net force in the gradient direction. Inside the contraction ($-6.6 \leq x_1 \leq 6.6$), $\sigma_{11} - \sigma_{22}$ increases to a maximum of 13.6, 14.0, and 15.4 for the linear, star, and branched molecules, respectively.

An analysis on the conformational changes of the systems is now carried out to associate the molecular structure to the rheological response. The shape of the molecule is associated to the principal axes (eigenvalues of the mass distribution tensor, $\left(\left\langle I_1^2\right\rangle, \left\langle I_2^2\right\rangle\right.$, and $\left.\left\langle I_3^2\right\rangle\right)$ which circumscribe the distribution of the segments in the directions x_1, x_2, and x_3 (the square of the radius of gyration is the sum of the squares of the three eigenvalues). Generally, the segments of a molecule are distributed primarily along the major axis of the ellipsoid $\left(\left\langle I_1^2\right\rangle\right)$, with reduced presence along the other axes. For Lc_1 / $Lc_2 = 1$, Fig. 10 shows the variation of the eigenvalue $\left\langle I_3^2\right\rangle$ as a function of x_1 for the linear, star, and branched molecules. The branched molecule possesses low segmental distribution along the neutral direction, which is related to high extensional viscosity (see Fig. 6).

It is generally accepted that the flow of polymers through contraction–expansion experience uniaxial elongation at the contraction and a biaxial expansion at the exit, that is, an elongation–relaxation process. This is corroborated by the variation of $\left\langle I_3^2\right\rangle$ shown in Fig. 10. For example, for the star molecule, $\left\langle I_3^2\right\rangle$ goes through a minimum prior to the contraction (see curve labeled 1) and grows at the exit (see 5), showing the deformation–relaxation process. Between points (1) and (5), two biaxial expansions (from 1 to 2, and from 3 to 4) and two uniaxial elongations (from 2 to 3 and from 4 to 5) are implied. These conformation changes are associated to the observed peaks in pressure drop and rate of dissipation shown in Fig. 8.

The shear stress is closely related to the rate of dissipation through the contraction (Castillo-Tejas et al. 2009) and, hence, to the pressure drop. The variation of the shear stress $\sigma_{21}(x_2)$ prior to the contraction ($-41.4 \leq x_1 \leq -6.6$) goes from zero along the symmetry line and grows as the walls are approached, with a maximum located at the reentrant corner, whose magnitude depends on the molecular structure (0.96, 1.19, and 2.13 for the linear, star, and branched molecules, respectively). This behavior of the shear stress (not shown) influences the total pressure drop for Lc_1 / $Lc_2 = 1$.

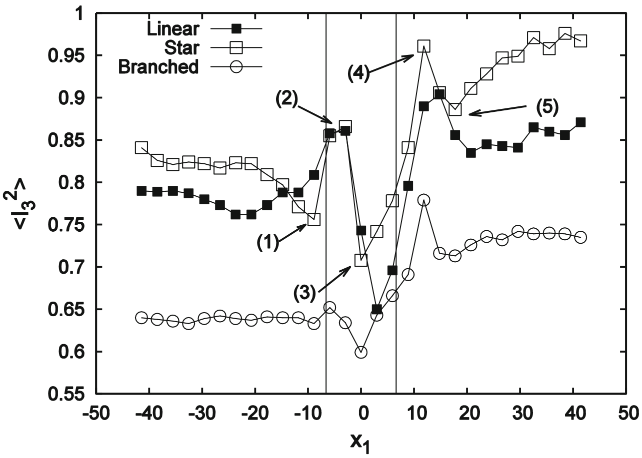

Fig. 10 Reduced mass distribution tensor eigenvalue $\left\langle I_3^2\right\rangle$ as a function of the axial coordinate x_1 for polymer melts at $Q \approx 50$

In some works (Doyle et al. 1998; Rothstein and McKinley 2002), a close relationship between the hysteresis cycles of stress conformation and rate of dissipation is suggested. In Fig. 11, a stress–conformation hysteresis cycle is predicted for the three polymers at the reference flow rate. The cycle is expressed in terms of the stress difference $\sigma_{11} - \sigma_{22}$ and the mean-squared radius of gyration $\left\langle R_g^2\right\rangle$. For Lc_1 / $Lc_2 = 1$, the enclosed area is larger in the linear molecules than in the branched ones, revealing that the hysteresis area is not directly related to the rate of dissipation or pressure drop. However, upon increasing Lc_1 / Lc_2 to 1.3 for the linear molecules, the area increases and so as the rate of dissipation.

Extensional rheology in dilute solution

The excess pressure drop observed in axisymmetric geometries is related to the dimensions of the contraction itself (contraction ratio), and here, we can manipulate the ratio Lc_1 / Lc_2 in planar geometries to obtain a similar effect. As shown in Fig. 6, $\Delta P(Q)$ is similar for the Newtonian and dilute solutions for Lc_1 / $Lc_2 = 1$ and augments upon increasing Lc_1 / Lc_2. Excess pressure drops along contraction–expansion geometries are usually presented in terms of the ratio of the excess pressure drop (ΔP_{Entry}) originated by the reduction in flow area to the pressure drop under steady flow conditions. Thus,

$$\Delta P_{\text{Entry}} = \Delta P - \Delta P_0 - \Delta P_1 \tag{12}$$

where ΔP is the total pressure drop (see Fig. 6), and ΔP_0 and ΔP_1 are the pressure drops under steady flow conditions prior and past the contraction, respectively. (ΔP_{Entry}) represents the additional pressure drop that the fluid experiences through the contraction. To obtain the pressure drops

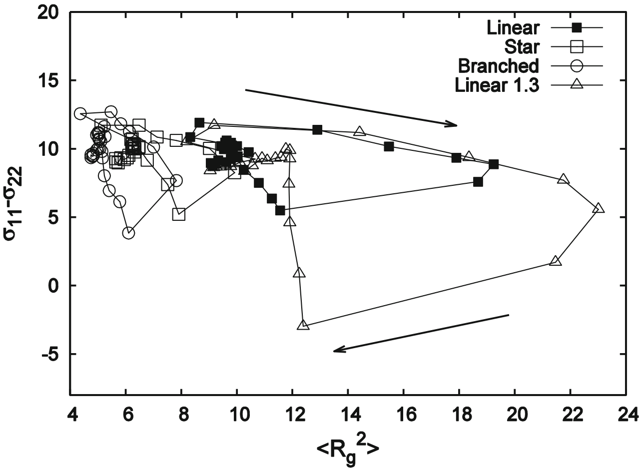

Fig. 11 Reduced stress difference $\sigma_{11} - \sigma_{22}$ as a function of reduced radius of gyration $\left\langle R_g^2\right\rangle$ for polymer melts at $Q \approx 50$

$(\Delta P_0,\ \Delta P_1)$, steady flow conditions are here defined as those corresponding to the test region where the molecular conformation is not modified by the contraction. With regard to the behavior of $\left\langle I_3^2 \right\rangle$ (see Fig. 14), steady flow is predicted along the test region for $x_1 = j20j$. Hence, the nondimensional pressure drop is defined as follows:

$$\Delta P_{\mathrm{Adim}} = \Delta P_{\mathrm{Entry}}(Q) \big/ \Delta P_{\mathrm{Entry-LJ}}(Q) \qquad (13)$$

where $\Delta P_{Entry}(Q)$ is the pressure drop experienced by solution at a given flow rate, and $\Delta P_{Entry-LJ}(Q)$ is that experienced by L-J Fluid at the same flow conditions. In Fig. 12, ΔP_{Adim} (the excess pressure drop with respect to the reference fluid) is plotted with the flow rate. An initial decrease of ΔP_{Adim} gives values lower than the reference fluid, but for larger flow rates, positive increases are predicted. Likewise, positive increases upon the reference value are reached as the contraction ratio Lc_1 / Lc_2 increases. These results illustrate the right trend that ΔP_{Adim} should have as the flow area decreases and reveals that changes in the geometrical ratio of the contraction may lead to large effects on the extensional viscosity and, hence, on the pressure drop.

Figure 13 presents the strain rate $\overset{\bullet}{\varepsilon} = \Delta v_1 \big/ \Delta x_1$ calculated along the symmetry line $x_2 = 0$ as a function of the axial coordinate x_1. For $x_1 \leq -30$, the fluid velocity is constant, increasing up to a maximum at the contraction entry zone. For Lc_1 / Lc_2 = 1, the L-J fluid and the dilute solution exhibit same strain rate. Past the maximum, Δv_1 / Δx_1 goes through two minima at $x_1 \approx 0$ and $x_1 \approx 20$, associated to a diminishing velocity. Notice that upon increasing the ratio Lc_1 / Lc_2 to 1.3 and 1.6 in the dilute solution originates larger strain rates at the entrance and exit of the contraction, and hence, larger pressure drops. As mentioned, Fig. 13a shows a maximum and a minimum in $\overset{\bullet}{\varepsilon}$ located at the entrance of the contraction at $x_1 \approx 20$. Both peaks are consistent with the strain rate obtained in the works of Li et al. (2011a, b). However, in this work, we predict additional important variations in $\overset{\bullet}{\varepsilon}$ located between the mentioned maximum and minimum. This may be associated with the resolution inherent in the molecular dynamics technique.

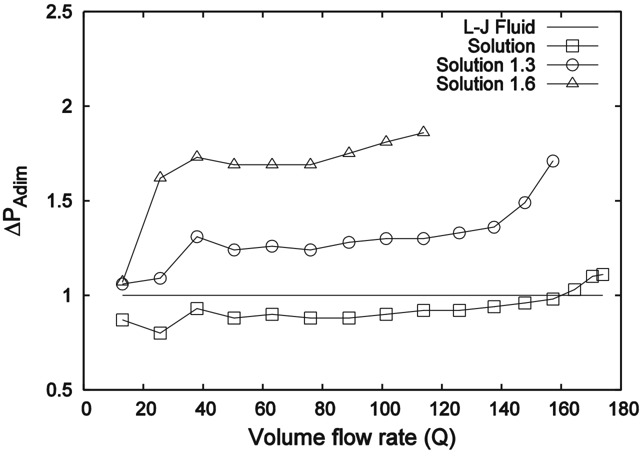

Fig. 12 Reduced pressure drop ΔP_{Adim} as a function of volume flow rate Q for the L-J fluid and the solution of linear molecules with different ratios Lc_1 / Lc_2

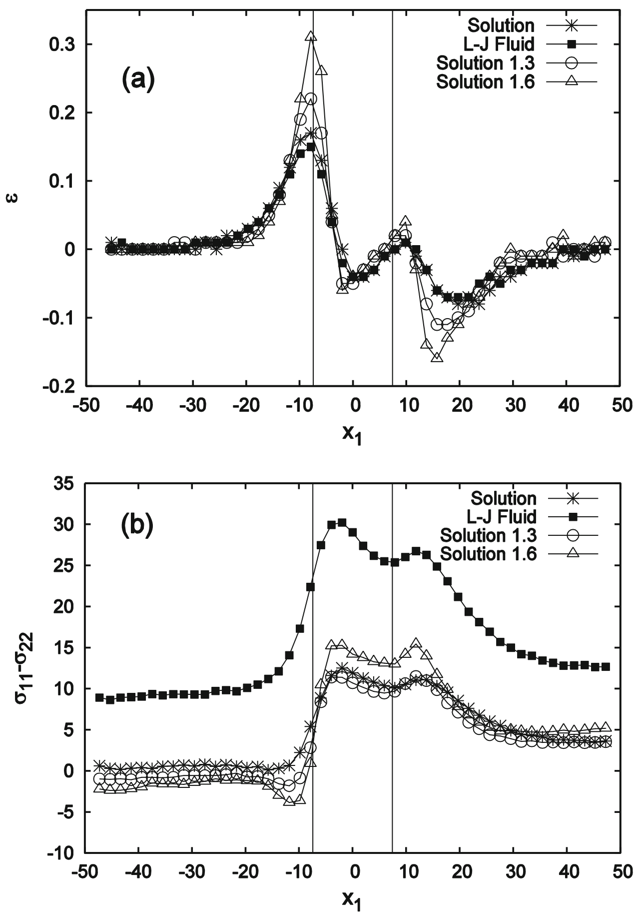

Fig. 13 **a** Variation of reduced strain rate $\dot{\varepsilon} = \Delta v_1/\Delta x_1$ obtained from velocities profiles at $x_2 = 0$, and **b** reduced stress difference $\sigma_{11} - \sigma_{22}$ as a function of the axial coordinate x_1 at $Q \approx 100$ for diluted solution and L-J fluid

In Fig. 13b, the variation of $\sigma_{11} - \sigma_{22}$ is plotted as a function of the axial coordinate x_1 for the dilute solution and the L-J fluid, and for various Lc_1 / Lc_2 ratios. Results shown in Fig. 12 reveal that the *epd* for the dilute solution (upon increasing the ratio Lc_1 / Lc_2) is associated to larger strain rate and rate of dissipation. Results for a planar geometry are consistent with the criteria pointed out by Walters et al. (2009) and Tamaddon-Jahromi et al. (2011) for axisymmetric geometries. These criteria relate the *epd* with a balance of extensional viscosity η_E and N_1. A weaker than quadratic dependence of N_1 with the shear rate and high extensional viscosity promote larger *epd* values.

In Fig. 14a, the axial dependence of the segment distribution along the neutral direction $\langle I_3^2 \rangle$ is illustrated. Upon increasing the strain rate by augmenting the ratio Lc_1 / Lc_2, $\langle I_3^2 \rangle$ and $\langle I_2^2 \rangle$ diminish in the solution. For example, at the maximum of Δv_1 / Δx_1, the molecules in the solution present $\langle I_3^2 \rangle$ values of 0.56, 0.53, and 0.50 for Lc_1 / Lc_2 ratios of 1.0, 1.3, and 1.6, respectively. An interesting observation is the fact that, in contrast to the molecules of the melt, the molecules in solution exhibit a single deformation–relaxation process. Major deformations occur at the entrance of the contraction, as $\langle I_3^2 \rangle$ and $\langle I_2^2 \rangle$ (not shown) go through a minimum and $\langle I_1^2 \rangle$ increases up to a maximum (not shown), in fact following a uniaxial deformation. Relaxation defined here as a biaxial expansion manifests through an increase in segment distribution along the axes x_2 and x_3, coinciding with a decrease along x_1. Finally, Fig. 14b corroborates the effect of the ratio Lc_1 / Lc_2 upon the molecular conformation in terms of the hysteresis cycles. Again, upon increasing the ratio Lc_1 / Lc_2, the subtended area increases.

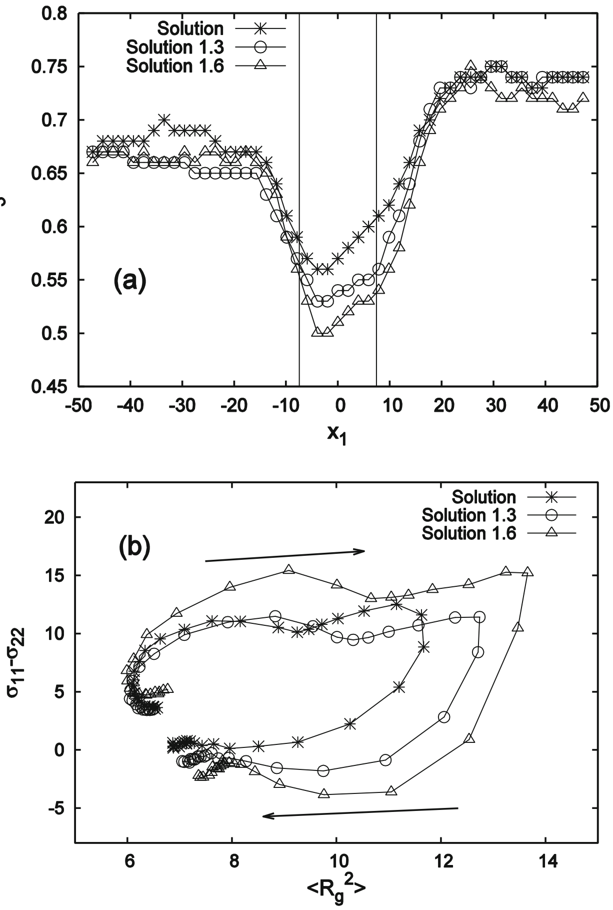

Fig. 14 **a** Reduced mass distribution tensor eigenvalue $\langle I_3^2 \rangle$ as a function of the axial coordinate x_1, and **b** reduced stress difference $\sigma_{11} - \sigma_{22}$ as a function of radius of gyration $\langle R_g^2 \rangle$, for diluted solution at different Lc_1 / Lc_2

Conclusions

In this work, the flow of molecules of various conformations through a planar 2:1:2 contraction–expansion geometry was analyzed in detail, applying periodic boundary conditions with minimum image along the neutral and flow directions. Two fluids were considered: shear thinning and constant viscosity liquids. The shear-thinning fluids comprised three melts with similar zero shear-rate viscosity η_0. The constant viscosity fluids included a dilute solution and a reference L-J fluid, both with similar η_0.

Polymer melts

For a ratio of Lc_1 / Lc_2 = 1.0, the pressure profile $P(x_1)$ and the total pressure drop ΔP depend on the branching index, such that, upon increasing the index, the pressure drop augments. The branched molecules (BI = 11.54) exhibit the largest pressure gradient ΔP / Δx_1 along the flow direction. However, by modifying the ratio Lc_1 / Lc_2, ΔP may be larger in molecules with lower branching index.

The rate of dissipation E_v and the energy removed by the thermostat U_{NHT} allow establishing their equality, as a first approximation, indicating that the thermostat is consistent with energy conservation. On the basis of this equivalence, the rate of dissipation $U_{NH}(k)$, strain rate $\dot{\varepsilon} = \Delta v_1 \Big/ \Delta x_1$, and the stress difference $\sigma_{11} - \sigma_{22}$ are closely related to the pressure gradient ΔP / Δx_1. The molecular conformation analysis indicates that, in the high pressure drop region, melts experience multiple deformation–relaxation processes. The branched molecules produce larger pressure gradients, as the distribution of segments along the gradient and neutral directions changes substantially. The geometrical ratio Lc_1 / Lc_2 is an important parameter with high influence upon the resulting pressure drop, as revealed by the work required to deform the molecules measured in terms of the hysteresis cycles.

Solution and L-J fluid

Results in planar geometries indicate that upon increasing Lc_1 / Lc_2, the solution of molecules exhibits larger pressure drops than that of the reference L-J fluid with Lc_1 / $Lc_2 = 1$, both fluids of similar viscosity. Results presented here signal a major effect of the geometric parameters. Changing the ratio Lc_1 / Lc_2 in planar contraction–expansions (reducing the flow area of the contraction) leads to similar strain rates observed in axisymmetric geometries. For Lc_1 / Lc_2 = 1, the L-J fluid and the dilute solution present the same pressure drop assigned to similar deformations and rate of dissipation. Upon increasing Lc_1 / Lc_2, the dilute solution presents *epd* caused by larger strain rate. The stress difference $\sigma_{11} - \sigma_{22}$ with weaker than quadratic dependence on the shear rate is associated to the *epd* observed in the solution.

Under flow conditions, the product $\lambda \dot{\varepsilon}$ is related to the drag force that experiences a chain segment, for example, in the dumbbell model for $\lambda \dot{\varepsilon} < 0.5$, the force between bonds dominates, and the molecule possesses a coil conformation (Larson 1999). At the fully developed region prior to the contraction, the product $\lambda \dot{\varepsilon}$ has a mean value of 4.28, indicating the importance of the drag forces and, therefore, of the strain rate. The above discussion allows the possibility that in axisymmetric geometries, the net force on the molecules drags them toward the central confining line, in larger proportions than in the case of planar geometries. This in turn develops larger extensional stresses and pressure drops.

Acknowledgments The authors are grateful for the financial support from SEP-CONACyT, PROMEP and Universidad Autónoma de Tlaxcala through the projects CB-2008/100195, PROMEP/103.5/12/2116, and CACyPI-UATx-2013, respectively.

References

Aboubacar M, Matallah H, Tamaddon-Jahromi HR, Webster MF (2002) Numerical prediction of extensional flows in contraction geometries: hybrid finite volume/element method. J Non-Newton Fluid Mech 104:125–164

Aguayo JP, Tamaddon-Jahromi HR, Webster MF (2008) Excess pressure-drop estimation in contraction and expansion flows for constant shear-viscosity, extension strain-hardening fluids. J Non-Newton Fluid Mech 153:157–176

Alves MA, Oliveira PJ, Pinho FT (2003) Benchmark solutions for the flow of Oldroyd-B and PTT fluids in planar contractions. J Non-Newton Fluid Mech 110:45–75

Binding DM (1988) An approximate analysis for contraction and converging flows. J Non-Newton Fluid Mech 27:173–189

Binding DM (1991) Further considerations of axisymmetric contraction flows. J Non-Newton Fluid Mech 41:27–42

Binding DM, Walters K (1988) On the use of flow through a contraction in estimating the extensional viscosity of mobile polymer solutions. J Non-Newton Fluid Mech 30:233–250

Binding DM, Phillips PM, Phillips TN (2006) Contraction/expansion flows: the pressure-drop and related issues. J Non-Newton Fluid Mech 137:31–38

Bird R, Armstrong R, Hassager O (1987) Dynamics of polymeric liquids, volume I. Wiley, New York

Busic B, Koplik J, Banavar JR (2003) Molecular dynamics simulation of liquid bridge extensional flows. J Non-Newtonian Fluid Mech 109:51–89

Campo-Deaño L, Galindo-Rosales F, Pinho FT, Alves MA, Oliveira MSN (2011) Flow of low viscosity Boger fluids through a microfluidic hyperbolic contraction. J Non-Newtonian Fluid Mech 166:1286–1296

Campo-Deaño L, Galindo-Rosales FJ, Pinho FT, Alves MA, Oliveira MSN (2012) Nanogel formation of polymer solutions flowing through porous media. Soft Matter 8:6445–6453

Castillo-Tejas J, Alvarado JFJ, González-Alatorre G, Luna-Barcenas G, Sanchez IC, Macias-Salinas R, Manero O (2005) Non-equilibrium molecular dynamics of the rheological and structural properties of linear and branched molecules. Simple shear and Poiseuille flows; instabilities and slip. J Chem Phys 123(5):054907

Castillo-Tejas J, Rojas-Morales A, López-Medina F, Alvarado JFJ, Luna-Barcenas G, Bautista F, Manero O (2009) Flow of linear molecules through a 4:1:4 contraction-expansion using non-equilibrium molecular dynamics: extensional rheology and pressure drop. J Non-Newton Fluid Mech 161:48–59

Daivis PJ, Evans DJ, Morriss GP (1992) Computer simulation study of the comparative rheology of branched and linear alkanes. J Chem Phys 97:616–627

Delhommelle J, Petravic J, Evans DJ (2003) Reexamination of string phase and shear thickening in simple fluids. Phys Rev E 68(031201):1–6

Delhommelle J, Petravic J, Evans DJ (2004) Non-Newtonian behavior in simple fluids. J Chem Phys 120:6117–6123

Doyle PS, Shaqfeh ESG, McKinley GH, Spiegelberg SH (1998) Relaxation of dilute polymer solutions following extensional flow. J Non-Newton Fluid Mech 76:79–110

Evans D, Morriss G (1990) Statistical mechanics of non-equilibrium liquids. Academic, New York

Flyvbjerg H, Petersen HC (1989) Error estimates on averages of correlated data. J Chem Phys 91:461–466

Gabriel C, Munstedt H (2003) Strain hardening of various polyolefins in uniaxial elongational flow. J Rheol 47:619–630

Genieser L, Brown RA, Armstrong RC (2003) Comparison of measured center-plane stress and velocity fields with predictions of viscoelastic constitutive models. J Rheol 47:1331–1350

González-González G, Castillo-Tejas J, Aguayo-Vallejo JP, Alvarado JFJ, Manero O (2009) Predictions of the excess pressure drop of Boger fluids through a 2:1:2 contraction-expansion geometry using non-equilibrium molecular dynamics. Rheol Acta 48:1017–1030

Gotsis AD, Zeevenhoven BLF (2004) Effect of long branches on the rheology of polypropilene. J Rheol 48:895–914

Haile JM (1997) Molecular dynamics simulation. Wiley, New York

Haward SJ, Odell JA, Li Z, Yuan XF (2010a) Extensional rheology of dilute polymer solutions in oscillatory cross-slot flow: the transient behaviour of birefringent strands. Rheol Acta 49:633–645

Haward SJ, Odell JA, Li Z, Yuan XF (2010b) The rheology of polymer solution elastic strands in extensional flow. Rheol Acta 49:781–788

Haward SJ, Li Z, Lighter D, Thomas B, Odell JA, Yuan X-F (2010c) Flow of dilute to semidilute polystyrene solutions through a benchmark 8:1 planar micro-contraction. J Non-Newton Fluid Mech 165:1654–1669

Haward SJ, Oliveira MSN, Alves MA, McKinley GH (2012a) Optimized cross-slot flow geometry for microfluidic extensional rheometry. Phys Rev Lett 128301:109

Haward SJ, Ober TJ, Oliveira MSN, Alves MA, McKinley GH (2012b) Extensional rheology and elastic instabilities of a wormlike micellar solution in a microfluidic cross-slot device. Soft Matt 8:536–555

Jabbarzadeh A, Atkinson JD, Tanner RI (2003) Effect of molecular shape on rheological properties in molecular dynamics simulation of star, H, comb, and linear polymer melts. Macromolecules 36:5020–5031

Kremer K, Grest G (1990) Dynamics of entangled linear polymer melts: a molecular-dynamics simulation. J Chem Phys 92:5057–5086

Lanzaro A, Yuan X-F (2011) Effects of contraction ratio on non-linear dynamics of semi-dilute, highly polydisperse PAAm solutions in microfluidics. J Non-Newton Fluid Mech 166:1064–1075

Larson RG (1999) The structure and rheology of complex fluids. Oxford University Press, New York

Le Tu C, Todd BD, Daivis PJ, Uhlherr A (2009a) The effect of interbranch spacing on structural and rheological properties of hyperbranched polymer melts. J Chem Phys 131(12):164901

Le Tu, C, Todd BD, Daivis PJ, Uhlherr A (2009b) Rheology of hyperbranched polymer melts undergoing planar Couette flow. J Chem Phys 131(10):044902

Li Z, Yuan XF, Haward SJ, Odell JA, Yeates S (2011a) Non-linear dynamics of semi-dilute polydisperse polymer solutions in microfluidics: a study of a benchmark flow problem. J Non-Newtonian Fluid Mech 166:951–963

Li Z, Yuan XF, Haward SJ, Odell JA, Yeates S (2011b) Non-linear dynamics of semi-dilute polydisperse polymer solutions in microfluidics: effects of flow geometry. Rheol Acta

Lubansky AS, Boger DV, Servais C, Burbidge AS, Cooper-White JJ (2007) An approximate solution to flow through a contraction for high Trouton ratio fluids. J Non-Newton Fluid Mech 144:87–97

Mazur J, Guttman CM, McCracking FL (1973) Monte Carlo studies of self-interacting polymer chains with excluded volume. II. Shape of a chain. Macromolecules 6:872–874

Moller D, Munstedt H, Kaspar H (2009) Rheological behaviour and molecular structure of long-chain branched semifluorinated thermoplastics. Rheol Acta 48:509–516

Moore JD, Cui ST, Cochran HD, Cummings PT (2000) A molecular dynamics study of a short chain polyethylene melt. I. Steady state shear. J Non-Newtonian Fluid Mech 93:83–99

Neelov IM, Adolf DB (2003) Brownian dynamics simulation of dendrimers under elongational flow: bed-rod model with hydrodynamic interactions. Macromolecules 36:6914–6924

Neelov IM, Adolf DB (2004) Brownian dynamics simulation of hyperbranched polymers under elongational flow. J Phys Chem B 108:7627–7636

Nigen S, Walters K (2002) Viscoelastic contraction flows: comparison of axisymmetric and planar configurations. J Non-Newton Fluid Mech 102:343–359

Nose S (1984) A unified formulation of the constant temperature molecular dynamics methods. J Chem Phys 81:511–519

Ogura K, Takahashi M (2003) Uniaxial and biaxial behavior of a lightly cross linked PMMA melt at constant rates. J Soc Rheol Jpn 31:79–83

Rapaport DC (2004) The art of molecular dynamics simulation. Cambridge University Press, Cambridge

Rodd LE, Cooper-White JJ, Boger DV, McKinley GH (2005) The inertio-elastic planar entry flow of low-viscosity elastic fluids in micro-fabricated geometries. J Non-Newton Fluid Mech 129:1–22

Rodd LE, Cooper-White JJ, Boger DV, McKinley GH (2007) Role of the elasticity number in the entry flow of diluted polymer solutions in micro-fabricated contraction geometries. J Non-Newton Fluid Mech 143:170–191

Rothstein JP, McKinley GH (1999) Extensional flow of a polystyrene Boger fluid through a 4:1:4 axisymmetric contraction/expansion. J Non-Newton Fluid Mech 86:61–88

Rothstein JP, McKinley GH (2001) The axisymmetric contraction-expansion: the role of extensional rheology on vortex growth dynamics and the enhanced pressure drop. J Non-Newton Fluid Mech 98:33–63

Rothstein JP, McKinley GH (2002) Inhomogeneous transient uniaxial extensional rheometry. J Rheol 46:1419–1443

Szabo P, Rallison JM, Hinch EJ (1997) Start-up of flow of a FENE-fluid through a 4:1:4 constriction in a tube. J Non-Newton Fluid Mech 72:73–86

Sendijarevic I, McHugh A (2000) Effects of molecular variables and architecture on the rheological behavior of dendritic polymers. Macromolecules 33:590–596

Tamaddon-Jahromi HR, Webster MF, Walters K (2010) Predicting numerically the large increases in extra pressure drop when Boger fluids flow through axisymmetric contractions. Nat Sci 2:1–10

Tamaddon-Jahromi HR, Webster MF, Williams PR (2011) Excess pressure drop and drag calculations for strain-hardening fluids with mild shear-thinning: contraction and falling spheres problems. J Non-Newton Fluid Mech 166:939–950

Todd B, Evans D, Daivis P (1995) Pressure tensor for inhomogeneous fluids. Phys Rev E 52:1627–1638

Wagner MH (2004) Relating rheology and molecular structure of model branched polystyrene melts by molecular stress function theory. J Rheol 48:489–503

Walters K, Webster MF (2003) The distinctive CFD challenges of computational rheology. Int J Numer Methods Fluids 43:577–596

Walters K, Webster MF, Tamaddon-Jahromi HR (2009) The numerical simulation of some contraction flow of a highly elastic liquids and their impact on the relevance of the Couette correction in extensional rheology. Chem Eng Sci 64:4632–4639

Wapperom P, Keunings R (2001) Numerical simulation of branched polymer melts in transient complex flow using Pom-Pom models. J Non-Newton Fluid Mech 97:267–281

Warner Jr HR (1972) Kinetic theory and rheology of dilute suspensions of finitely extensible dumbbells. Ind & Eng Chem Fundam 11:379–387

Woods-Adams P, Dealy J, deGroot A, Redwine O (2000) Effect of molecular structure on the linear viscoelastic behavior of polyethylene. Macromolecules 33:7489–7499

Xu Z, dePablo JJ, Kim S (1995) Transport properties of polymer melts from nonequilibrium molecular dynamics. J Chem Phys 102:5836–5844

Xu Z, Khare R, dePablo JJ, Kim S (1997) On the calculation of transport properties of polymer melts from nonequilibrium molecular dynamics. J Chem Phys 106:8285–8286

Zhang Z, Hansen JS, Todd BD (2007) Structural and dynamical properties for confined polymers undergoing planar Poiseuille flow. J Chem Phys 126(1–14):144907